THE JOURNAL OF PHYSICAL CHEMISTRY LETTERS
A JOURNAL OF THE AMERICAN CHEMICAL SOCIETY

pubs.acs.org/JPCL
Letter

Unraveling the Nature of Vibrational Dynamics in $CsPbI_3$ by Inelastic Neutron Scattering and Molecular Dynamics Simulations

Rasmus Lavén, Erik Fransson, Paul Erhart, Fanni Juranyi, Garrett E. Granroth, and Maths Karlsson*

Cite This: J. Phys. Chem. Lett. 2025, 16, 4812−4818

ABSTRACT: Cesium lead iodide, $CsPbI_3$, is an optoelectronic material of large interest for various technological applications; however, fundamental questions surrounding the vibrational dynamics of this material, especially regarding its role in structural phase transitions, remain to be elucidated. Here, in a combined variable temperature inelastic neutron scattering (INS) and machine-learning based molecular dynamics (MD) simulation study, we show that the stable phase at room temperature, i.e., the nonperovskite δ-phase, exhibits phonon modes with weak anharmonicity with only a weak temperature dependence from 10 K all the way up to the transition to the cubic perovskite α-phase at approximately 600 K. In contrast, the α-phase features anharmonic and damped vibrational dynamics, mainly associated with overdamped tilting motions of the PbI_6 octahedra. Crucially, these overdamped tilting modes, which relate to the tetragonal and orthorhombic distorted perovskite phases (β- and γ-phase, respectively) formed at lower temperatures, stay overdamped by more than 100 K above the respective phase transition. This suggests a flat energy landscape of octahedral tilting motions in α-$CsPbI_3$ and with structural fluctuations on the picosecond time scale with tilting patterns that locally resemble the structure of the β- and γ-phases. The vibrational dynamics of α-$CsPbI_3$ are also characterized by pronounced anharmonic motions with large thermal displacements of the Cs^+ ions, but these modes remain underdamped at 600 K.

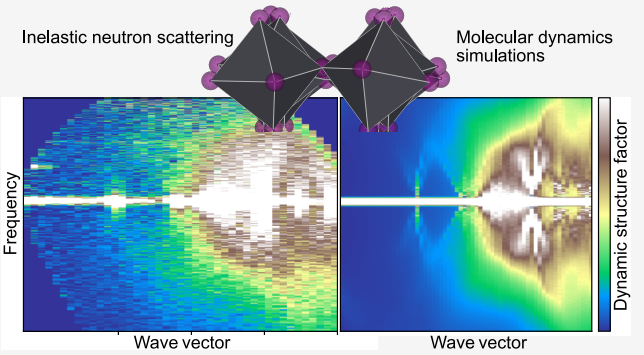

Metal halide perovskites (MHPs), i.e., materials of the form ABX_3, where A and B are cations and X is a halide anion, are a class of materials that have gained great attention in recent years for their promise in optoelectronic applications, such as solar panels and lighting.[1,2] On a fundamental level, one of the general characteristics of these materials is their generally "soft" nature, with typically unusually large thermal displacements of the constituting atoms. Early studies suggested that these large thermal displacements are present mainly in hybrid organic−inorganic MHPs and are related to dynamics of the organic cations, which express themselves as various reorientational motions.[3] However, more recent works have shown that large thermal displacements seem to be generally present also in all-inorganic MHPs, such as $CsPbBr_3$[4] and have, in part, been related to soft and, typically, overdamped vibrational dynamics in these materials. Such soft, or overdamped dynamics, are commonly observed in the vicinity of displacive phase transitions of many materials, such as, e.g., $SrTiO_3$,[5] $BaTiO_3$,[6] $LiNbO_3$,[7] and $CsPbCl_3$.[8] As one lowers the temperature and moves away from the phase transition into the lower symmetry crystal phase, these soft modes "freeze in" and become static, giving rise to the elastic Bragg scattering of the supercell reflections in the lower-symmetry phase. Crucially, overdamped vibrational dynamics in MHPs have also been related to the formation of large polarons and screening of charge carriers, defect tolerance, moderate charge carrier mobility, and low radiative recombination rates, that are of high importance for MHPs in actual applications.[9,10] This suggests that the vibrational dynamics in MHPs are a key to understanding the underpinning mechanisms of their optoelectronic properties. The current understanding of the nature of vibrational dynamics, especially overdamped dynamics and its relevance for optoelectronic properties in MHPs, comes mostly from INS, Raman spectroscopy, and computer simulations.[4,11−15] Phase transitions and dynamics in halide perovskites have been studied prior using computational and theoretical methods.[16−20] With regard to all-inorganic MHPs, most work has been focused on $CsPbBr_3$, for which an INS study on a single crystal sample unraveled overdamped vibrational dynamics related to $PbBr_6$ octahedral tilting motions at the M and R points of the Brillouin zone that, in turn, relate to the cubic-to-tetragonal

Received: March 14, 2025
Revised: April 30, 2025
Accepted: April 30, 2025
Published: May 8, 2025

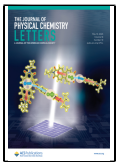

https://doi.org/10.1021/acs.jpclett.5c00778
J. Phys. Chem. Lett. 2025, 16, 4812−4818

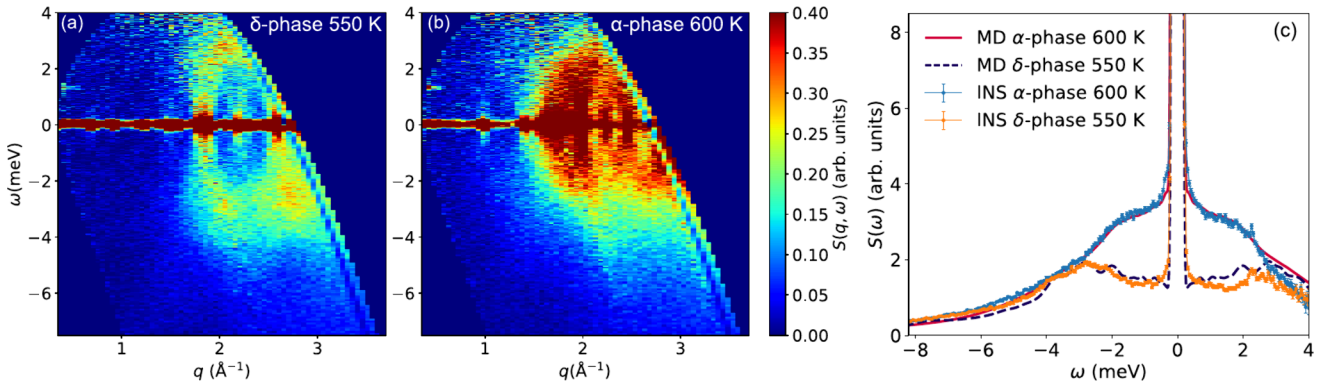

Figure 1. $S(q, \omega)$ of δ-$CsPbI_3$ (a) and α-$CsPbI_3$ (b), as measured on FOCUS. The small peak at 1.33 meV for very small q ($\lesssim$0.5 Å^{-1}) is a spurious peak from the instrument. (c) Comparison of the experimental and simulated $S(\omega)$, here summed over all measured q values (~0.2 to 3.5 Å^{-1}). The MD simulated data is convoluted with a Gaussian of fwhm = 0.15 meV to mimic the contribution of the instrumental resolution in the experimental data.

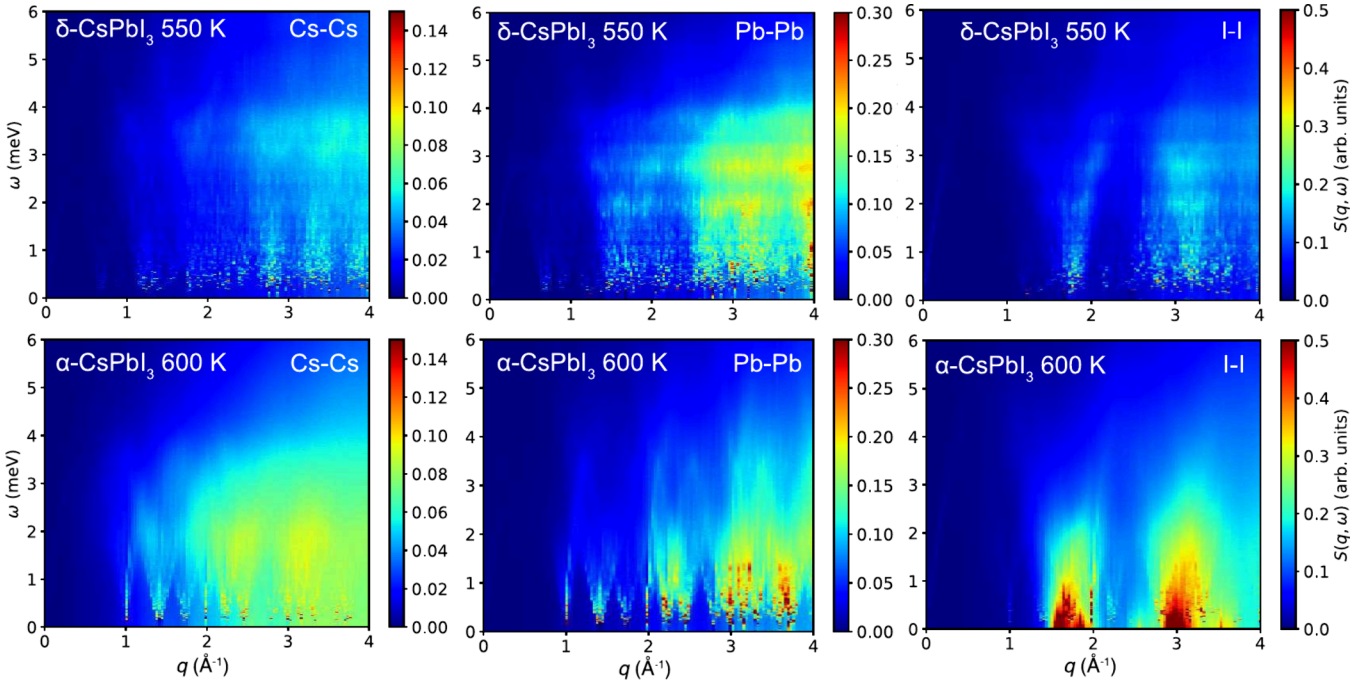

Figure 2. Partial dynamic structure factors of δ-$CsPbI_3$ at 550 K (top panels) and α-$CsPbI_3$ at 600 K (bottom panels) as derived from MD simulations. Note that the different elements are plotted on different scales for $S(q, \omega)$. The elastic data point at $\omega = 0$ is removed from the data.

and tetragonal-to-orthorhombic phase transitions, respectively.[15] Recently, some of us showed by MD simulations that these octahedral tilting motions stay overdamped far above the phase transition temperature,[21] which is related to the flat energy landscape present in the cubic perovskite phase of $CsPbX_3$ (X = I, Br).[11,12,22−26] However, the theoretical work[21] requires consolidation and, in particular, motivates further research aimed at unraveling whether these results are also applicable to other MHP materials. In this work, we thus investigate the nature of vibrational dynamics in the halide-ion-substituted material $CsPbI_3$ over a large temperature range from 10 to 600 K, using a combination of INS and MD simulations. $CsPbI_3$ adopts an orthorhombic (δ) nonperovskite phase (space group *Pnma*) at room temperature, which transforms to a cubic (α) perovskite phase (space group $Pm\bar{3}m$), i.e., the optically active phase, upon heating to around 600 K.[12] By cooling from 600 K, the material has been shown to transform to a tetragonal (β) phase (space group *P4/mbm*) at 554 K and to an orthorhombic (γ) phase (space group *Pnma*) at 457 K,[12] although it should be noted that the direct transition upon cooling from the α-phase to the δ-phase has also been observed.[27]

Up to now, the only experimental reports on the vibrational dynamics in $CsPbI_3$ are based on results from Raman spectroscopy measurements; however, these are in most cases limited to the study of symmetry-allowed optical vibrational modes at the center of the Brillouin zone.[28−32] In our work, this is mitigated by the use of INS since INS is sensitive to all vibrational modes in a material and, furthermore, can be compared to MD simulation data on an absolute scale. In effect, this means that INS data can provide a stringent test of the calculated local structures and dynamics present in the material. The combined analyses of variable temperature INS and MD simulation data thus allow us to unravel the nature of vibrational dynamics of $CsPbI_3$ and how it changes with temperature. The INS experiments were

https://doi.org/10.1021/acs.jpclett.5c00778
J. Phys. Chem. Lett. 2025, 16, 4812−4818

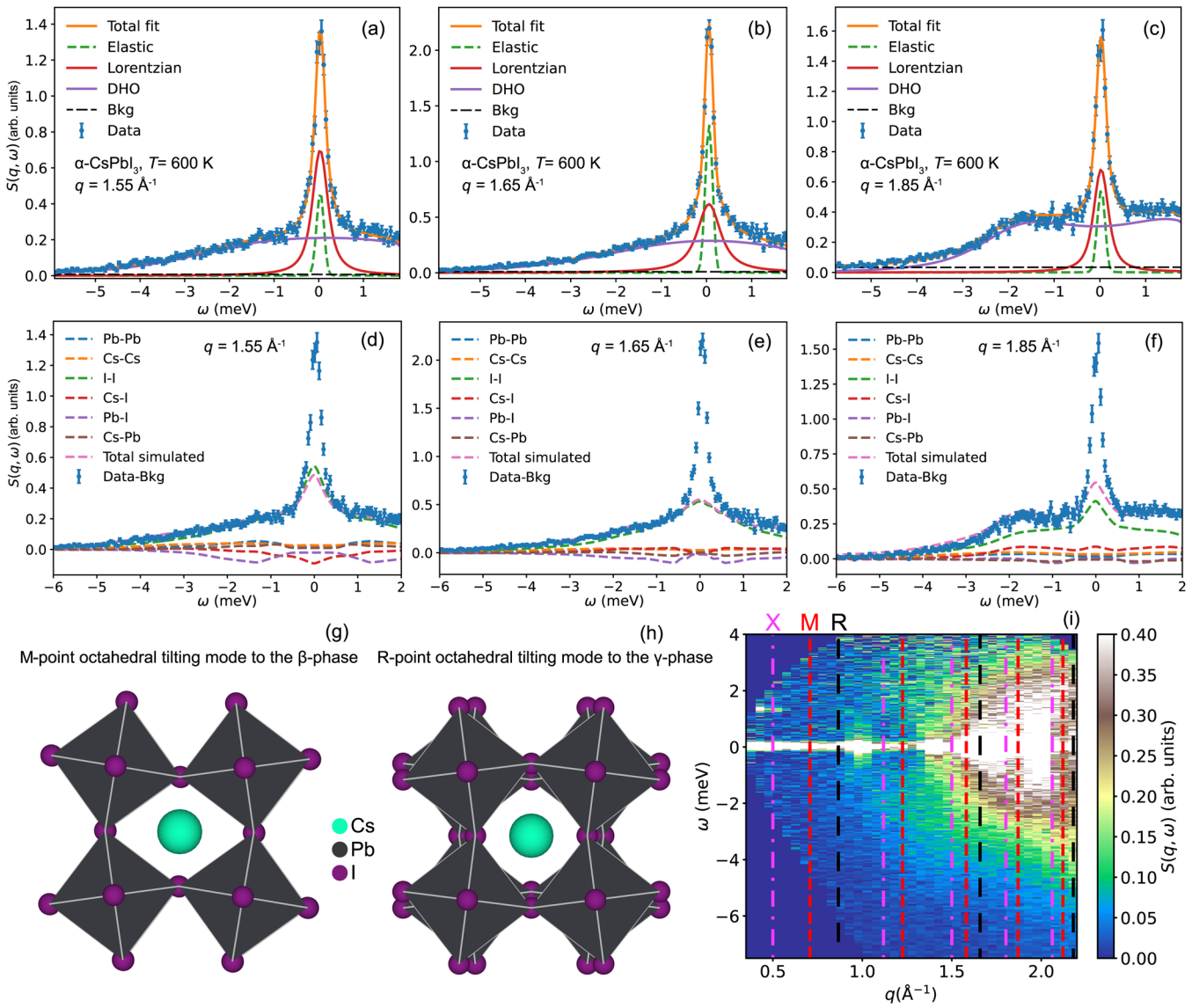

Figure 3. (a–c) $S(q, \omega)$ of α-$CsPbI_3$ at 600 K together with fits for q = 1.55 Å^{-1} and 1.65 Å^{-1} and 1.85 Å^{-1}. The data was measured on FOCUS. (d–f) Same data as in (a–c) but compared to the partial $S(q, \omega)$ from the MD simulations. The MD simulated data is convoluted with a Gaussian of fwhm = 0.15 meV to mimic the contribution of the instrumental resolution in the experimental data. The higher elastic scattering in the experimental data is due to incoherent elastic scattering which is not considered in the simulation (see Figure S11). (g–h) Illustration of the octahedral tilting mode at the M- and R-points. Note that, for the M-point mode, the layers tilt in the same direction, while for the R-point mode, the alternating layers tilt in alternating directions. The figures are made using VESTA.[35] (i) $S(q, \omega)$ of α-$CsPbI_3$ at 600 K with the modulus of different high-symmetry points of the cubic Brillouin zone (X, M, R) marked as dashed lines.

carried out on a powder sample of $CsPbI_3$, from which we derived the dynamical structure factor $S(q, \omega)$, where ω and q are, respectively, the energy transfer and modulus of the wavevector transfer; see the Methods section for details about the experiments and MD simulations.

Figure 1 compares the experimental dynamical structure factor $S(q, \omega)$ for the nonperovskite (δ) phase (at 550 K) and the cubic perovskite (α) phase of $CsPbI_3$ (at 600 K). Figure S2 shows the corresponding $S(q)$, which confirms the δ-to-α phase transition between 550 and 600 K. For both phases, $S(q, \omega)$ is characterized by strong, q-dependent, coherent scattering. For the nonperovskite phase, δ-$CsPbI_3$, this coherent scattering is manifested as acoustic phonon scattering, which disperses from the (212) Bragg peak at around q = 1.85 Å^{-1}[33] up to about 3 meV, whereas essentially no phonon scattering is observed below q = 1.85 Å^{-1}. These phonons exhibit only a weak temperature dependence from 10 K up to the phase transition to the α-phase around 600 K (see Figure S6). For the perovskite phase, α-$CsPbI_3$, acoustic phonon scattering dispersing out from the Bragg peaks can be also observed, with low intensity of the phonon scattering below the (110) Bragg peak at approximately q = 1.4 Å^{-1}. However, a striking difference between the two phases is the marked increase in the level of low-energy, virtually quasielastic scattering for α-$CsPbI_3$. This is further evident in Figure 1c, which compares the q-integrated $S(q, \omega)$ for both phases of $CsPbI_3$. Included in this graph is the simulated $S(q, \omega)$, as obtained from MD simulations for both phases and at the same temperatures. We observe excellent agreement between the experimental and simulated data, providing strong support that the simulated $S(q, \omega)$ can be used to gain detailed insight into the underlying dynamics.

https://doi.org/10.1021/acs.jpclett.5c00778
J. Phys. Chem. Lett. 2025, 16, 4812–4818

Since it is very unlikely that α-$CsPbI_3$ possesses any translational and/or rotational diffusional dynamics and due to the strong q-dependence, the quasielastic scattering signal suggests the presence of relaxational dynamics associated with either strongly damped and/or overdamped phonon dynamics. To investigate the origin of the dynamics giving rise to quasi-elastic scattering, we compare the experimental $S(q, \omega)$ to the computed partial dynamical structure factors for the Cs−Cs, Pb−Pb, and I−I correlations for both δ-$CsPbI_3$ (at 550 K) and α-$CsPbI_3$ (at 600 K; Figure 2). For α-$CsPbI_3$, the partial dynamical structure factors are manifested by quasi-elastic scattering due to I−I correlations, whereas dynamics associated with Cs−Cs and Pb−Pb correlations are generally characterized by higher energies and are less pronounced. Notably, the quasielastic scattering due to I−I correlations is concentrated to the q-ranges of about 1.5 $Å^{-1}$ to 1.9 $Å^{-1}$ and 2.85 $Å^{-1}$ to 3.2 $Å^{-1}$, which suggests that the dynamics are associated with overdamped octahedral tilting modes at the M and R points of the Brillouin zone. This is supported by the calculated current correlations along the high-symmetry directions (Figure S17), which shows overdamped modes along the M−R lines in the Brillouin zone. This is in full accordance with earlier studies of $CsPbBr_3$.[15,21] Note, the cross-correlation terms (Cs−I, Pb−I, and Cs−Pb) are generally slightly smaller than the noncross terms over the whole probed wavevector range, although it should be noted that also the Cs−I correlations contribute to the quasielastic scattering at 1.5 $Å^{-1}$ to 1.9 $Å^{-1}$ and 2.85 $Å^{-1}$ to 3.2 $Å^{-1}$ (Figures S14 and S15).

Figure 3a−c shows fits to the $S(q, \omega)$ spectra of α-$CsPbI_3$ at q = 1.55 $Å^{-1}$, 1.65 $Å^{-1}$, and 1.85 $Å^{-1}$ (the q-integration range is ±0.05 $Å^{-1}$). The two first q-values correspond to the values close to the modulus of $\mathbf{M} = \frac{2\pi}{a}\left(\frac{3}{2}, \frac{1}{2}, 0\right)$, i.e., $|\mathbf{M}|$ = 1.58 $Å^{-1}$ and $\mathbf{R} = \frac{2\pi}{a}\left(\frac{3}{2}, \frac{1}{2}, \frac{1}{2}\right)$, i.e., $|\mathbf{R}|$ = 1.66 $Å^{-1}$. The third q-value corresponds to a value close to the modulus of both $\mathbf{X} = \frac{2\pi}{a}\left(\frac{3}{2}, 1, 0\right)$, i.e., $|\mathbf{X}|$ = 1.8 $Å^{-1}$, and $\mathbf{M} = \frac{2\pi}{a}\left(\frac{3}{2}, \frac{1}{2}, 1\right)$, i.e., $|\mathbf{M}|$ = 1.87 $Å^{-1}$. It implies that the data in Figure 3a−c contain a large contribution from phonons at these high-symmetry points, although it must be noted that also phonons at all other reciprocal lattice vectors of the same modulus will contribute to the spectra. An illustration of the parts of q-space probed with the powder INS at q = 1.55 $Å^{-1}$ and q = 1.85 $Å^{-1}$ is shown in Figure S12.

At q = 1.55 $Å^{-1}$ (Figure 3a), i.e., at the M-point of the Brillouin zone, the quasielastic contribution to $S(q, \omega)$ can be adequately fitted to one Lorentzian function with a spectral line width of 0.32 meV at full width at half-maximum (fwhm). The remaining inelastic scattering can be approximated by a damped harmonic oscillator (DHO) function. However, since we measured on a powder sample and, therefore, measure the average of $S(q, \omega)$ over all wavevector directions, the DHO component will correspond to an average of many phonons lying close in energy and not related to a single real dynamical process; therefore, we do not analyze the DHO component further in this work. The Lorentzian component is assigned to octahedral tilting motions, with a relaxational time of $2\hbar$/fwhm ≃ 4 ps, which, because of the quasielastic nature of the scattering, are overdamped in nature, in perfect agreement with the MD simulations; see Figure 3d−f for a comparison between MD simulated partial $S(q, \omega)$. The higher elastic scattering in the experimental data is due to incoherent elastic scattering, which is not considered in the simulation (see Figure S11).

Notably, these tilting modes are related to the α-to-β phase transition, which is expected to occur at ∼550 K for $CsPbI_3$,[12] so quasielastic scattering at the M-point is indeed expected near this temperature based on the soft-phonon model for displacive phase transitions.[34] Remarkably, however, we observe such quasielastic scattering about 50 K above the phase transition temperature, which consolidates the earlier MD simulation study on $CsPbBr_3$ in that the octahedral tilting motions are overdamped even far above (more than 100 K) the phase transitions.[21] A graphical illustration of the M-point mode is shown in Figure 3g.

Similarly to the data at q = 1.55 $Å^{-1}$, at q = 1.65 $Å^{-1}$ [Figure 3b], i.e., at the R-point of the Brillouin zone, the quasielastic scattering of $S(q, \omega)$ can be fitted to one Lorentzian component, but here, the Lorentzian function corresponds to slightly faster-time scale dynamics (2.4 ps). The tilting mode at R corresponds to the tilt observed at the phase transition to the orthorhombic (γ) phase, which is expected to occur around 450 K[12] (Figure 3h). In the soft phonon model, the line width would increase as one moves away from the critical temperature; thus, it is reasonable that the relaxational dynamics related to the quasielastic scattering is faster around R. Nevertheless, it is remarkable to observe the quasielastic scattering at 600 K, which is 150 K above the transition to the orthorhombic (γ) phase.

At q = 1.85 $Å^{-1}$ (Figure 3c), the overdamped dynamics feature a relaxation time of 4.7 ps, which is similar to the overdamped dynamics associated with octahedral tilting motions at q = 1.55 $Å^{-1}$. In this context, we note that X point phonons are not expected to be soft close to the phase transitions; hence, they cannot be related to such a mode.[15] Instead, the relaxational dynamics observed here are most likely to come from scattering at the next M-point at $\frac{2\pi}{a}\left(\frac{3}{2}, \frac{1}{2}, 1\right)$, which is featured by a modulus of 1.87 $Å^{-1}$. As inferred from the partial $S(q, \omega)$ as calculated from the MD simulations [Figures 2 and 3f], in addition to the I−I correlations, the Cs−Cs and Cs−I correlations contribute more at this higher q-value. Consequently, these underdamped dynamics also contain a contribution from displacement of the Cs^+ ions. Detailed information about these dynamics can be obtained by comparing the partial dynamic structure factors. More specifically, the partial $S(q, \omega)$ for Cs−Cs correlations exhibits a sharp increase in intensity at around ≈1.6 $Å^{-1}$, above which it is roughly q-independent (incoherent). This gives evidence of low-energy (soft) spatially decoherent motions of the Cs^+ cations in the perovskite cage at 600 K.

With regard to the difference in vibrational dynamics between δ and α-$CsPbI_3$, we note that the average Pb−I bond lengths are almost the same in both phases (3.2 Å and 3.14 Å for δ- and α-phase, respectively) and the average Cs−I bond length on the other hand differs significantly (3.9 Å and 4.45 Å for the δ- and α-phase, respectively).[12,33] At the same time, the shortest average Pb−Cs distance is larger in the perovskite phase (4.92 Å and 5.45 Å for the δ- and α-phase, respectively). This could indicate a significantly different potential energy landscape for the Cs^+ ions in the perovskite phase, with a lower interaction potential and larger atomic displacements, which is in agreement with computational studies showing a flat energy landscape in perovskite $CsPbI_3$.[11,12] It also explains the large thermal displacement

https://doi.org/10.1021/acs.jpclett.5c00778
J. Phys. Chem. Lett. 2025, 16, 4812−4818

parameters of Cs (isotropic) and I (perpendicular to the Pb−I−Pb bonds) in the cubic perovskite phase, which was found to be significantly smaller in the orthorhombic δ-phase.[27] These large thermal displacements of I and Cs atoms would also mean that the distribution of bond lengths is much broader for Cs and I atoms in the cubic α-phase. A similar conclusion has been reached for isostructural $CsSnI_3$ for which it was found that the phase transition to the cubic perovskite phase is derived from the stabilization of "rattling" Cs^+ cations within the cubo-octahedral sites.[36] Interestingly, a recent study based on the analysis of X-ray pair distribution functions suggests that the rattling of Cs^+ ions, low number of Cs−I contacts, and high degree of octahedral distortion cause the instability of the perovskite phase $CsPbI_3$.[37] However, another study has shown that there is a well-defined phase relation between the Cs^+ dynamics and the PbI_6 framework dynamics in the orthorhombic γ-phase.[38] Here, we directly observe such behavior of Cs^+ cations in α-$CsPbI_3$. It is clear from the q-dependence of the partial Cs−Cs $S(q, \omega)$ from the MD data [cf. Figure 2 and Figure S9] that the dynamics of the Cs^+ cations become significantly more spatially incoherent in the α-phase compared to the δ-phase and also compared to the other atomic species in the material. However, one should note that the calculated $S(q, \omega)$ shows that the dynamics of Cs^+ cations, although heavily damped, remain underdamped in α-$CsPbI_3$.

The observation of quasielastic scattering related to overdamped dynamics of octahedral tilting motions in α-$CsPbI_3$ is in full accordance with our results for $CsPbBr_3$ (Figure S13), suggesting no strong dependence of the type of halide ion (X) on the overall vibrational dynamics in $CsPbX_3$ (X = I and Br). Furthermore, we note that the extracted relaxation time of the overdamped dynamics is about 4 ps, which means that the cubic α-phase of $CsPbI_3$ exhibits structural fluctuations with tilting patterns that locally resemble the tetragonal and orthorhombic distorted structures on the ps time scale.

To conclude, our INS and MD simulation studies of $CsPbI_3$ are in excellent agreement and have unraveled the nature of vibrational dynamics in the various phases of $CsPbI_3$. Crucially, we have shown that the stable phase at room temperature, i.e., in the nonperovskite δ-phase, exhibits vibrational dynamics with only a weak temperature dependence from 10 K all the way up to the transition to the cubic perovskite α-phase at approximately 600 K. In contrast, the α-phase features anharmonic and damped vibrational dynamics, mainly associated with overdamped tilting modes of PbI_6 octahedra, with relaxational times between 2 and 4 ps at 600 K. The overdamped dynamics highlight the flat energy landscape for octahedral tilting motions in α-$CsPbI_3$, even markedly above the phase transition temperature from lower symmetry distorted orthorhombic and tetragonal perovskite phases (γ- and β-phases, respectively), which thus give rise to dynamical fluctuations on the picosecond time scale in the α-phase. These dynamical fluctuations may explain the discrepancy found in the literature between the average cubic structure found by diffraction and the local, noncubic structure, as observed with total-scattering and spectroscopy techniques. Our results thus show that information about the vibrational dynamics can even provide crucial information for understanding the structure of these types of materials.

Finally, one should note that INS was performed on a powder sample, whereas the other INS studies on MHPs of this kind were performed on single crystal samples. While, in principle, the INS signal of a powder sample is less informative, since the signal is averaged over all q directions, the combination with MD simulations allows us to still draw detailed conclusions about the dynamics in the material. In effect, our results highlight that this approach can be applied to studies of other MHPs, as well as other solid-state materials, which may not be possible to synthesize as (large enough) single crystals. This is in particular true for the here studied material $CsPbI_3$, for which the presence of the thermodynamically stable nonperovskite δ-phase at room temperature makes the synthesis of single crystals of perovskite phase $CsPbI_3$ more challenging.[33]

Methods. *Experimental Details.* The INS experiments were carried out on the time-of-flight spectrometers FOCUS[39] at the Swiss Spallation Neutron Source SINQ and ARCS[40] at the Spallation Neutron Source in the U.S. The samples, $CsPbI_3$ and $CsPbBr_3$ powders, were held inside standard Al cylindrical shaped samples cells, which were kept unsealed to keep the samples under dynamic vacuum during the measurements; see Supporting Information (SI) for further details about the samples.

FOCUS was set up using an incident neutron wavelength of 4 Å (corresponding to an energy of 5.11 meV), which yielded an energy resolution at fwhm of approximately 0.2 meV and a wavevector transfer (q) range of 0.5 $Å^{-1}$ to 2.7 $Å^{-1}$ at the elastic line. Standard data reduction of the measured raw data was performed within the DAVE software[41] and included normalization to a vanadium standard, for detector efficiency correction, and subtraction of the scattering from an empty sample cell. ARCS was set up using incident neutron energies of 15, 30, and 50 meV, which provided corresponding energy resolutions at fwhm of 0.45, 0.9, and 1.5 meV at the elastic line. Standard data reduction of the measured raw data was performed within the Mantid software[42] and included the same corrections as for the FOCUS data. For both experiments, the computed response function is the dynamic structure factor $S(q, \omega)$. The energy and momentum transfer $E = \hbar\omega$ and $|\mathbf{p}| = \hbar q$ will be used interchangeably with ω and q.

The quasielastic scattering from overdamped dynamics in $S(q, \omega)$ was fitted to a Lorentzian centered around $\omega = 0$. In addition to the Lorentzian component, an elastic scattering component, described by a delta function convoluted with the instrumental resolution function (as here determined by a measurement of a vanadium standard), a DHO function used to describe the remaining inelastic scattering, and a constant background (Bkg) were included in the fitting. The Lorentzian and DHO components were also convoluted with the instrumental resolution function in the fitting.

Computational Details. The experimental $S(q, \omega)$ was compared to the simulated $S(q, \omega)$ as obtained from the MD simulations. The MD simulations were carried out with the GPUMD package.[43,44] The atomic interactions were modeled using a machine-learned potential of the neuroevolution potential (NEP) form, which was constructed in ref 45. This NEP model accurately reproduces energies, forces, and virials from density functional theory calculations based on the vdW-DF-cx functional.[46,47] A time step of 2 fs was used in the MD simulations. The lattice parameters were determined through *NPT* simulations, after which $S(q, \omega)$ was obtained from *NVE* simulations. In order to sample many different $\boldsymbol{q}$-points and mimic the experimental results, the $S(q, \omega)$s were averaged over about 20 different system sizes, ranging from 5000 to 4 50 000 atoms. The coherent part of the dynamical structure

https://doi.org/10.1021/acs.jpclett.5c00778
J. Phys. Chem. Lett. 2025, 16, 4812−4818

factors $S(\boldsymbol{q}, \omega)$ was obtained from the Fourier transform of the intermediate scattering function, $F(\boldsymbol{q}, t)$, which was calculated from the MD trajectories using the DYNASOR package[48] as

$$F(\mathbf{q}, t) = \sum_{i}^{N} \sum_{j}^{N} \langle b_i b_j \exp[i\mathbf{q}\cdot(\mathbf{r}_i(t) - \mathbf{r}_j(0))]\rangle$$

Here, $\langle\cdots\rangle$ indicates an ensemble average, N is the number of atoms, $\boldsymbol{r}_i(t)$ is the position of atom i at time t, and b_i is the bound coherent neutron scattering length of atom i. The latter is related to the coherent neutron cross section through $\sigma_{\text{coh}} = 4\pi b_i^2$. Since the average incoherent scattering cross section of the nuclei present in $CsPbI_3$ is more than a factor 20 smaller than the coherent part, the incoherent dynamical structure $S(q, \omega)_{\text{inc}}$ was neglected in the calculation. We employed spherical q-point sampling in the range of 0 $Å^{-1}$ to 5 $Å^{-1}$, but we note that the accuracy of $S(q, \omega)$ at $q \lesssim 0.2$ $Å^{-1}$ is limited by the finite system size in the MD simulations. For each system size, five independent MD simulations were carried out, each spanning 1 ns. Additionally we also compute the current correlations, $C(\boldsymbol{q}, \omega)$, for both the α- and δ-phase. The current correlation is based on the velocity autocorrelation function and consists of a transverse and a longitudinal part. The longitudinal part is directly related to the dynamical structure factor via

$$S(\boldsymbol{q}, \omega) = \frac{q^2}{\omega^2} C_L(\boldsymbol{q}, \omega) \quad (1)$$

The current correlation functions are computed with about 2 00 000 atoms along the high-symmetry $\boldsymbol{q}$-point path of the respective phase and from 7.5 ns long MD simulations.

■ ASSOCIATED CONTENT

Supporting Information

The Supporting Information is available free of charge at https://pubs.acs.org/doi/10.1021/acs.jpclett.5c00778.

Additional experimental details; supplementary INS and MD simulation data (PDF)

■ AUTHOR INFORMATION

Corresponding Author

Maths Karlsson − *Department of Chemistry and Chemical Engineering, Chalmers University of Technology, SE-412 96 Göteborg, Sweden;* orcid.org/0000-0002-2914-6332; Email: maths.karlsson@chalmers.se

Authors

Rasmus Lavén − *Department of Chemistry and Chemical Engineering, Chalmers University of Technology, SE-412 96 Göteborg, Sweden;* orcid.org/0000-0001-8165-461X

Erik Fransson − *Department of Physics, Chalmers University of Technology, SE-412 96 Göteborg, Sweden;* orcid.org/0000-0001-5262-3339

Paul Erhart − *Department of Physics, Chalmers University of Technology, SE-412 96 Göteborg, Sweden;* orcid.org/0000-0002-2516-6061

Fanni Juranyi − *Laboratory for Neutron Scattering and Imaging, PSI Center for Neutron and Muon Sciences, 5232 Villigen, Switzerland;* orcid.org/0000-0002-3223-072X

Garrett E. Granroth − *Neutron Scattering Division, Neutron Sciences Directorate, Oak Ridge National Laboratory, Oak Ridge, Tennessee 37831, United States*

Complete contact information is available at: https://pubs.acs.org/10.1021/acs.jpclett.5c00778

Notes

The authors declare no competing financial interest.

■ ACKNOWLEDGMENTS

This research was funded by the Swedish Research Council (Grant Nos. 2016-06958, 2018-06482, 2020-04935, 2021-05072) and the Chalmers Initiative for Advancement of Neutron and Synchrotron Techniques. This work is based on experiments performed at the Swiss Spallation Neutron Source SINQ, Paul Scherrer Institute, Villigen, Switzerland. A portion of this research used resources at the Spallation Neutron Source, a DOE Office of Science User Facility operated by the Oak Ridge National Laboratory. The computations were enabled by resources provided by the National Academic Infrastructure for Supercomputing in Sweden (NAISS) and the Swedish National Infrastructure for Computing (SNIC) at C3SE, NSC, HPC2N, and PDC partially funded by the Swedish Research Council through grant agreements no. 2022-06725 and no. 2018-05973.

■ REFERENCES

(1) Correa-Baena, J. P.; Abate, A.; Saliba, M.; Tress, W.; Jesper Jacobsson, T.; Grätzel, M.; Hagfeldt, A. The rapid evolution of highly efficient perovskite solar cells. *Energy Environ. Sci.* **2017**, *10*, 710−727.

(2) Jeon, N. J.; Noh, J. H.; Yang, W. S.; Kim, Y. C.; Ryu, S.; Seo, J.; Seok, S. I. Compositional engineering of perovskite materials for high-performance solar cells. *Nature* **2015**, *517*, 476−480.

(3) Chen, T.; Foley, B. J.; Ipek, B.; Tyagi, M.; Copley, J. R. D.; Brown, C. M.; Choi, J. J.; Lee, S.-H. Rotational dynamics of organic cations in the $CH_3NH_3PbI_3$ perovskite. *Phys. Chem. Chem. Phys.* **2015**, *17*, 31278−31286.

(4) Yaffe, O.; Guo, Y.; Tan, L. Z.; Egger, D. A.; Hull, T.; Stoumpos, C. C.; Zheng, F.; Heinz, T. F.; Kronik, L.; Kanatzidis, M. G.; Owen, J. S.; Rappe, A. M.; Pimenta, M. A.; Brus, L. E. Local Polar Fluctuations in Lead Halide Perovskite Crystals. *Phys. Rev. Lett.* **2017**, *118*, 1−6.

(5) Fleury, P. A.; Scott, J. F.; Worlock, J. M. Soft Phonon Modes and the 110°K Phase Transition in $SrTiO_3$. *Phys. Rev. Lett.* **1968**, *21*, 16−19.

(6) Harada, J.; Axe, J. D.; Shirane, G. Neutron-Scattering Study of Soft Modes in Cubic $BaTiO_3$. *Phys. Rev. B* **1971**, *4*, 155−162.

(7) Johnston, W. D.; Kaminow, I. P. Temperature Dependence of Raman and Rayleigh Scattering in $LiNbO_3$ and $LiTaO_3$. *Phys. Rev.* **1968**, *168*, 1045−1054.

(8) Fujii, Y.; Hoshino, S.; Yamada, Y.; Shirane, G. Neutron-scattering study on phase transitions of $CsPbCl_3$. *Phys. Rev. B* **1974**, *9*, 4549−4559.

(9) Miyata, K.; Atallah, T. L.; Zhu, X. Y. Lead halide perovskites: Crystal-liquid duality, phonon glass electron crystals, and large polaron formation. *Sci. Adv.* **2017**, *3*, 1−11.

(10) Zhu, H.; Miyata, K.; Fu, Y.; Wang, J.; Joshi, P. P.; Niesner, D.; Williams, K. W.; Jin, S.; Zhu, X.-Y. Screening in crystalline liquids protects energetic carriers in hybrid perovskites. *Science* **2016**, *353*, 1409−1413.

(11) Marronnier, A.; Lee, H.; Geffroy, B.; Even, J.; Bonnassieux, Y.; Roma, G. Structural Instabilities Related to Highly Anharmonic Phonons in Halide Perovskites. *J. Phys. Chem. Lett.* **2017**, *8*, 2659−2665.

(12) Marronnier, A.; Roma, G.; Boyer-Richard, S.; Pedesseau, L.; Jancu, J.-M.; Bonnassieux, Y.; Katan, C.; Stoumpos, C. C.; Kanatzidis, M. G.; Even, J. Anharmonicity and Disorder in the Black Phases of Cesium Lead Iodide Used for Stable Inorganic Perovskite Solar Cells. *ACS Nano* **2018**, *12*, 3477−3486.

(13) Hehlen, B.; Bourges, P.; Rufflé, B.; Clément, S.; Vialla, R.; Ferreira, A. C.; Ecolivet, C.; Paofai, S.; Cordier, S.; Katan, C.; Létoublon, A.; Even, J. Pseudospin-phonon pretransitional dynamics in lead halide hybrid perovskites. *Phys. Rev. B* **2022**, *105*, 024306.
(14) Songvilay, M.; Giles-Donovan, N.; Bari, M.; Ye, Z.-G.; Minns, J. L.; Green, M. A.; Xu, G.; Gehring, P. M.; Schmalzl, K.; Ratcliff, W. D.; Brown, C. M.; Chernyshov, D.; van Beek, W.; Cochran, S.; Stock, C. Common acoustic phonon lifetimes in inorganic and hybrid lead halide perovskites. *Phys. Rev. Materials* **2019**, 3, 093602.
(15) Lanigan-Atkins, T.; He, X.; Krogstad, M.; Pajerowski, D.; Abernathy, D.; Xu, G. N.; Xu, Z.; Chung, D.-Y.; Kanatzidis, M.; Rosenkranz, S. others. Two-dimensional overdamped fluctuations of the soft perovskite lattice in $CsPbBr_3$. *Nat. Mater.* **2021**, *20*, 977−983.
(16) Jinnouchi, R.; Lahnsteiner, J.; Karsai, F.; Kresse, G.; Bokdam, M. Phase Transitions of Hybrid Perovskites Simulated by Machine-Learning Force Fields Trained on the Fly with Bayesian Inference. *Phys. Rev. Lett.* **2019**, *122*, 225701.
(17) Chen, L.; Xu, B.; Yang, Y.; Bellaiche, L. Macroscopic and Microscopic Structures of Cesium Lead Iodide Perovskite from Atomistic Simulations. *Adv. Funct. Mater.* **2020**, *30*, 1909496.
(18) Wang, X.; Patel, K.; Prosandeev, S.; Zhang, Y.; Zhong, C.; Xu, B.; Bellaiche, L. Finite-Temperature Dynamics in Cesium Lead Iodide Halide Perovskite. *Adv. Funct. Mater.* **2021**, *31*, 2106264.
(19) Li, J.; Pan, F.; Zhang, G.-X.; Liu, Z.; Dong, H.; Wang, D.; Jiang, Z.; Ren, W.; Ye, Z.-G.; Todorović, M.; Rinke, P. Structural Disorder by Octahedral Tilting in Inorganic Halide Perovskites: New Insight with Bayesian Optimization. *Small Structures* **2024**, *5*, 2400268.
(20) Chen, G.-Y.; Guo, Z.-D.; Gong, X.-G.; Yin, W.-J. Kinetic pathway of γ-to-δ phase transition in $CsPbI_3$. *Chem.* **2022**, *8*, 3120−3129.
(21) Fransson, E.; Rosander, P.; Eriksson, F.; Rahm, J. M.; Tadano, T.; Erhart, P. Limits of the phonon quasi-particle picture at the cubic-to-tetragonal phase transition in halide perovskites. *Commun. Phys.* **2023**, *6*, 173.
(22) Wiktor, J.; Fransson, E.; Kubicki, D.; Erhart, P. Quantifying Dynamic Tilting in Halide Perovskites: Chemical Trends and Local Correlations. *Chem. Mater.* **2023**, *35*, 6737−6744.
(23) Baldwin, W. J.; Liang, X.; Klarbring, J.; Dubajic, M.; Dell'Angelo, D.; Sutton, C.; Caddeo, C.; Stranks, S. D.; Mattoni, A.; Walsh, A. others Dynamic Local Structure in Caesium Lead Iodide: Spatial Correlation and Transient Domains. *Small* **2024**, *20*, 2303565.
(24) Gu, H.-Y.; Yin, W.-J.; Gong, X.-G. Significant phonon anharmonicity drives phase transitions in $CsPbI_3$. *Appl. Phys. Lett.* **2021**, *119*, 191101.
(25) Klarbring, J. Low-energy paths for octahedral tilting in inorganic halide perovskites. *Phys. Rev. B* **2019**, *99*, 104105.
(26) Yang, R. X.; Skelton, J. M.; da Silva, E. L.; Frost, J. M.; Walsh, A. Spontaneous Octahedral Tilting in the Cubic Inorganic Cesium Halide Perovskites $CsSnX_3$ and $CsPbX_3$ (X = F, Cl, Br, I). *J. Phys. Chem. Lett.* **2017**, *8*, 4720−4726.
(27) Liu, J.; Phillips, A. E.; Keen, D. A.; Dove, M. T. Thermal Disorder and Bond Anharmonicity in Cesium Lead Iodide Studied by Neutron Total Scattering and the Reverse Monte Carlo Method. *J. Phys. Chem. C* **2019**, *123*, 14934−14940.
(28) Zhou, W.; Sui, F.; Zhong, G.; Cheng, G.; Pan, M.; Yang, C.; Ruan, S. Lattice dynamics and thermal stability of cubic-phase $CsPbI_3$ quantum dots. *J. Phys. Chem. Lett.* **2018**, *9*, 4915−4920.
(29) Yuan, G.; Qin, S.; Wu, X.; Ding, H.; Lu, A. Pressure-induced phase transformation of $CsPbI_3$ by X-ray diffraction and Raman spectroscopy. *Phase Transit* **2018**, *91*, 38−47.
(30) Liao, M.; Shan, B.; Li, M. In situ Raman spectroscopic studies of thermal stability of all-inorganic cesium lead halide ($CsPbX_3$, X= Cl, Br, I) perovskite nanocrystals. *J. Phys. Chem. Lett.* **2019**, *10*, 1217−1225.
(31) Yang, Y.; Robbins, J. P.; Ezeonu, L.; Ma, Y.; Sparta, N.; Kong, X.; Strauf, S.; Podkolzin, S. G.; Lee, S. S. Probing lattice vibrations of stabilized $CsPbI_3$ polymorphs via low-frequency Raman spectroscopy. *J. Mater. Chem. C* **2020**, *8*, 8896−8903.
(32) Satta, J.; Melis, C.; Carbonaro, C. M.; Pinna, A.; Salado, M.; Salazar, D.; Ricci, P. C. Raman spectra and vibrational analysis of $CsPbI_3$: A fast and reliable technique to identify lead halide perovskite polymorphs. *J. Materiomics* **2021**, *7*, 127−135.
(33) Straus, D. B.; Guo, S.; Cava, R. J. Kinetically Stable Single Crystals of Perovskite-Phase $CsPbI_3$. *J. Am. Chem. Soc.* **2019**, *141*, 11435−11439.
(34) Scott, J. F. Soft-mode spectroscopy: Experimental studies of structural phase transitions. *Rev. Mod. Phys.* **1974**, *46*, 83−128.
(35) Momma, K.; Izumi, F. VESTA 3 for Three-Dimensional Visulazation of Crystal, Volumetric and Morhpology Data. *J. Appl. Crystallogr.* **2011**, *44*, 1272−1276.
(36) Chung, I.; Song, J.-H.; Im, J.; Androulakis, J.; Malliakas, C. D.; Li, H.; Freeman, A. J.; Kenney, J. T.; Kanatzidis, M. G. $CsSnI_3$: Semiconductor or Metal? High Electrical Conductivity and Strong Near-Infrared Photoluminescence from a Single Material. High Hole Mobility and Phase-Transitions. *J. Am. Chem. Soc.* **2012**, *134*, 8579−8587.
(37) Straus, D. B.; Guo, S.; Abeykoon, A. M.; Cava, R. J. Understanding the Instability of the Halide Perovskite $CsPbI_3$ through Temperature-Dependent Structural Analysis. *Adv. Mater.* **2020**, *32*, 2001069.
(38) Thakur, S.; Giri, A. Origin of Ultralow Thermal Conductivity in Metal Halide Perovskites. *ACS Appl. Mater. Interfaces.* **2023**, *15*, 26755−26765.
(39) Janßen, S.; Mesot, J.; Holitzner, L.; Furrer, A.; Hempelmann, R. FOCUS: a hybrid TOF-spectrometer at SINQ. *Physica B* **1997**, *234*−*236*, 1174−1176.
(40) Abernathy, D. L.; Stone, M. B.; Loguillo, M. J.; Lucas, M. S.; Delaire, O.; Tang, X.; Lin, J. Y. Y.; Fultz, B. Design and operation of the wide angular-range chopper spectrometer ARCS at the Spallation Neutron Source. *Rev. Sci. Instrum.* **2012**, *83*, 015114.
(41) Azuah, R. T.; Kneller, L. R.; Qiu, Y.; Tregenna-Piggott, P. L.; Brown, C. M.; Copley, J. R.; Dimeo, R. M. DAVE: A comprehensive software suite for the reduction, visualization, and analysis of low energy neutron spectroscopic data. *J. Res. Natl. Inst. Stand. Technol.* **2009**, *114*, 341−358.
(42) Arnold, O.; et al. Mantid - Data analysis and visualization package for neutron scattering and μ SR experiments. *Nucl. Instruments Methods Phys. Res. Sect. A Accel. Spectrometers, Detect. Assoc. Equip.* **2014**, *764*, 156−166.
(43) Fan, Z.; Chen, W.; Vierimaa, V.; Harju, A. Efficient molecular dynamics simulations with many-body potentials on graphics processing units. *Comput. Phys. Commun.* **2017**, *218*, 10−16.
(44) Fan, Z.; et al. GPUMD: A package for constructing accurate machine-learned potentials and performing highly efficient atomistic simulations. *J. Chem. Phys.* **2022**, *157*, 114801.
(45) Fransson, E.; Wiktor, J.; Erhart, P. Phase Transitions in Inorganic Halide Perovskites from Machine-Learned Potentials. *J. Phys. Chem. C* **2023**, *127*, 13773−13781.
(46) Dion, M.; Rydberg, H.; Schröder, E.; Langreth, D. C.; Lundqvist, B. I. Van der Waals Density Functional for General Geometries. *Phys. Rev. Lett.* **2004**, *92*, 246401.
(47) Berland, K.; Hyldgaard, P. Exchange functional that tests the robustness of the plasmon description of the van der Waals density functional. *Phys. Rev. B* **2014**, *89*, 035412.
(48) Fransson, E.; Slabanja, M.; Erhart, P.; Wahnström, G. dynasor—A Tool for Extracting Dynamical Structure Factors and Current Correlation Functions from Molecular Dynamics Simulations. *Adv. Theory Simul.* **2021**, *4*, 2000240.

https://doi.org/10.1021/acs.jpclett.5c00778
J. Phys. Chem. Lett. 2025, 16, 4812−4818

Supporting Information:

Unraveling the nature of vibrational dynamics in $CsPbI_3$ by inelastic neutron scattering and molecular dynamics simulations

Rasmus Lavén,[1] Erik Fransson,[2] Paul Erhart,[2] Fanni Juranyi,[3] Garrett E. Granroth,[4] and Maths Karlsson[1]

[1]*Department of Chemistry and Chemical Engineering, Chalmers University of Technology, SE-412 96 Göteborg, Sweden.*

[2]*Department of Physics, Chalmers University of Technology, SE-412 96 Göteborg, Sweden.*

[3]*Laboratory for Neutron Scattering and Imaging, PSI Center for Neutron and Muon Sciences, Forschungsstrasse 111, 5232 Villigen, PSI, Switzerland*

[4]*Neutron Scattering Division, Neutron Sciences Directorate, Oak Ridge National Laboratory, Oak Ridge, Tennessee 37831, USA*

CONTENTS

S1. EXPERIMENTAL DETAILS

A. Samples

The samples, 12 g of $CsPbI_3$ powder (purity >99%) and 3 g of $CsPbBr_3$ powder (purity >99%), were purchased from Xi'an Polymer Light Technologies and used as received. The phase purity and crystallinity of the samples were confirmed at ambient temperature by powder X-ray diffraction. In addition, for $CsPbI_3$, the phase transition behaviour upon heating the sample from 293 to 650 K was checked using differential scanning calorimetry, which revealed a single endothermic peak at 601 K corresponding to the δ-α phase transition in accordance with the literature [S1, S2].

B. Inelastic neutron scattering

For the experiment on FOCUS we used 9 g of $CsPbI_3$ powder, loaded into a cylindrical 12.5 mm diameter Al sample holder. The measurements were performed using incident neutron wavelengths of 4 Å and 2 Å, respectively, which were obtained from the (002) and (004) Bragg reflections of the pyrolytic graphite monochromator. Using 4 Å incident wavelength neutrons provided an energy resolution at FWHM and wavevector transfer (q) range of approximately 0.2 meV and 0.5 to 2.7 $Å^{-1}$ at the elastic line. For 2 Å incident wavelength neutrons, the corresponding values were about 1 meV and 0.8 to 5.7 $Å^{-1}$, respectively. Measurements were taken at 50, 300, 400, 500, 550, and 600 K, in that order, with a measurement time of about 4 h per spectrum.

For the experiment on ARCS, we used 4 g of $CsPbI_3$ powder sample (from a different batch), loaded into a cylindrical 6.35 mm diameter Al sample holder. The measurements were performed using incident neutron energies of 15, 30, and 50 meV, which provided the corresponding energy resolutions at full width at half maximum (FWHM) of 0.45, 0.9, and 1.5 meV at the elastic line. Measurements were taken at 10, 300, 400, 495, 539, 564, 580, 595 and 610 K (on heating), and at 500 and 400 K (on cooling), with a measurement time of about 2 h per spectrum. Data reduction was done within the Mantid software [S3] and included normalization to a vanadium standard [S4] and subtraction of an empty sample cell measurement.

Both experiments, on FOCUS and ARCS, used a closed-cycle refrigerator with a high-temperature stage for temperature control. A recent publication from ARCS used the identical temperature controller as we did and we found a temperature-dependent offset between the temperature set point and actual temperature in the experiment [S5]. Using the expression for this offset, as reported in ref. [S5], we re-calibrated our temperature. It is likely that the temperature in the ARCS experiment was about 30 K lower at the highest measured temperature of 640 K, which is in agreement with the observed phase transition behaviour in our experiment. Similarly, for FOCUS, the temperature was re-calibrated by determining the cell parameter of the Al sample cell. Then, the temperature was calibrated to the predicted thermal expansion of Aluminium according to ref. [S6]. Figure S1 shows the re-calibrated temperature versus the read temperature for the FOCUS and ARCS experiment, respectively.

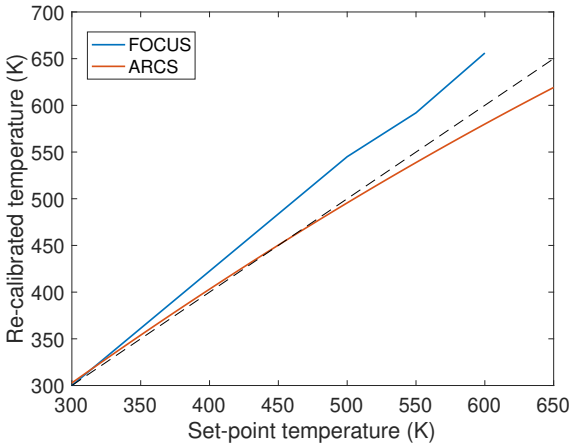

FIG. S1. Re-calibrated temperature versus the set-point temperature for the FOCUS and ARCS experiments. For comparison, the black dashed line has a slope 1.

S2. SUPPLEMENTARY INS DATA

A. Energy-integrated INS data

The studied crystal phases of $CsPbI_3$ during the INS measurements were further confirmed by the elastic Bragg scattering. Figure S2 shows the energy-integrated scattering in the low-q region, showing the Bragg scattering of $CsPbI_3$ for the measurements on ARCS and FOCUS. Upon heating, we observed the δ-α phase transition at around 600 K. Upon cooling ($\approx$ 4 K/min) from the α-phase, we observed the transition directly back to the $\delta-$phase around 540 K (Fig. S3). The phase transition behaviour as observed here is similar to the one reported by Liu *et al.* [S7], but different from other experiments [S8]. These differences may be related to different sample environments, experimental conditions, and sample to sample variations.

B. Generalized density of states

Figure S4 shows the generalized density of states (GDOS) of δ-$CsPbI_3$ at 300 and 550 K and α-$CsPbI_3$ at 600 K. The GDOS was derived from the INS data according to the incoherent approximation [S9, S10], *i.e.*

$$G(\omega) \propto \int \frac{\omega}{q^2} S(q,\omega)(1 - \mathrm{e}^{-\hbar\omega/k_\mathrm{B}T})\mathrm{d}q,$$

where k_B is Boltzmann's constant, $\hbar$ is the reduced Planck constant, and T is the temperature.

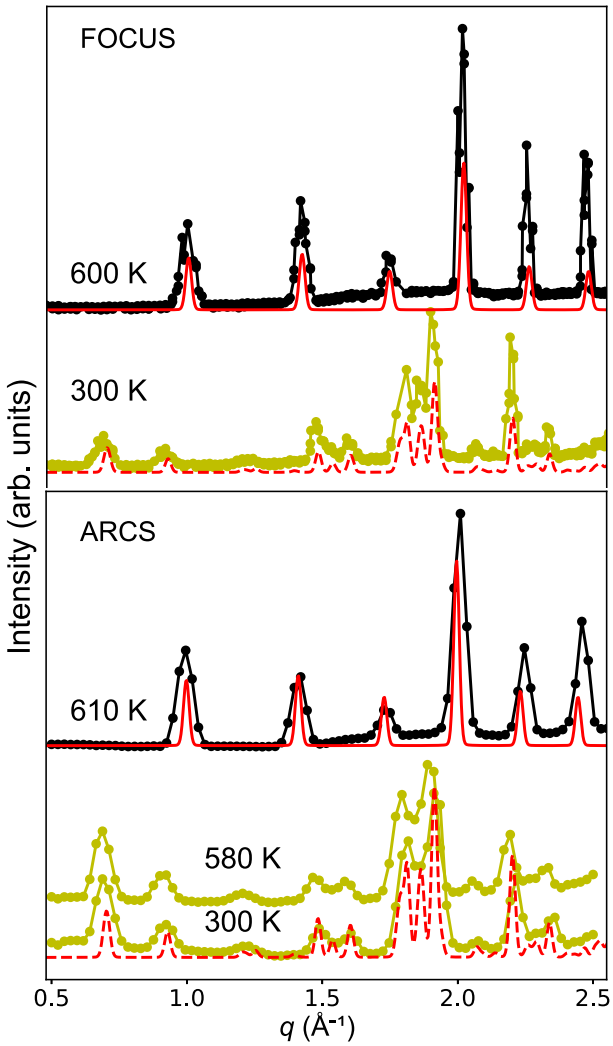

FIG. S2. Energy integrated scattering in the low-q region, as measured on FOCUS (upper panel) using an incident neutron wavelength of 4 Å, and on ARCS (lower panel) using an incident neutron energy of 15 meV, showing the δ-α phase transition. The data is compared to the simulated Bragg scattering of neutrons for the two different phases (dashed red lines for the δ-phase and full red lines for the α-phase). The increase in diffuse scattering for $q > 1.5$ Å^{-1} in the α-phase originates from inelastic scattering. The data sets have been separated vertically. The data were measured at ARCS using an incident neutron energy of 15 meV.

C. INS data with larger dynamical range

The INS data measured on ARCS with 15 meV incident neutron energy is shown in Fig. S5 for $\delta-CsPbI_3$ at 540 K and $\alpha-CsPbI_3$ at 610 K

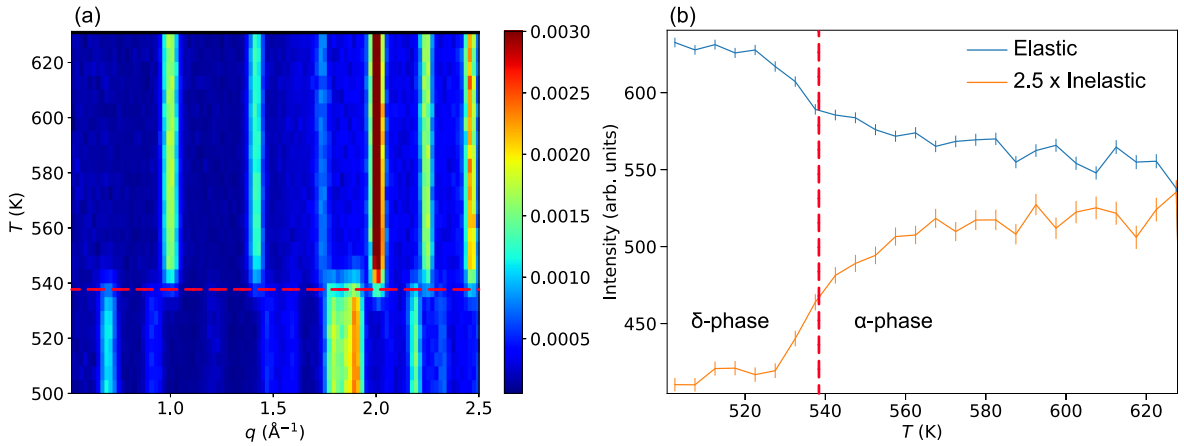

FIG. S3. (a) Energy integrated ($[-10, 10]$ meV) scattering in the low-q region, as measured on ARCS (left panel) using an incident neutron energy of 15 meV during cooling (4 K/min) from 620 K to 500 K. (b) Elastic scattering intensity (integrated over the interval $[-0.5, 0.5]$ meV) and inelastic scattering intensity (integrated over the interval $[0.7, 10]$ meV) integrated over the $q-$range $1-5$ Å^{-1}. The INS intensity is multiplied by a factor of 2.5 for increased visibility. The red dashed lines indicate approximately the transition temperature to the $\delta-$phase.

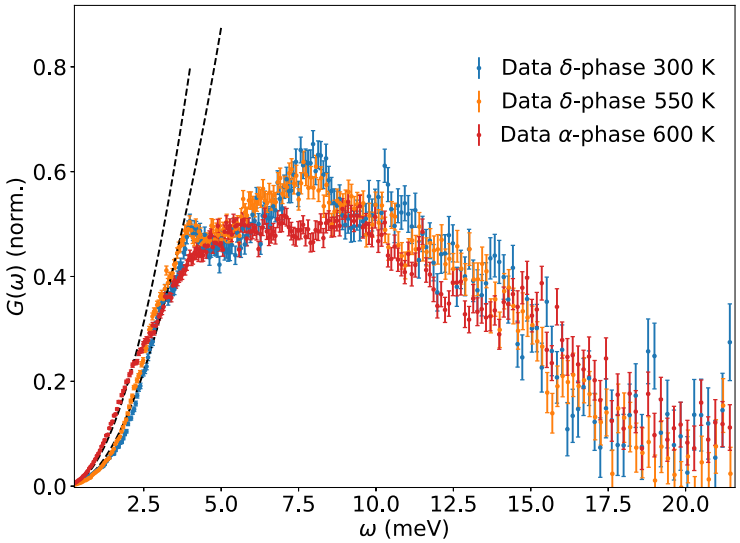

FIG. S4. GDOS of δ-$CsPbI_3$ (300 K and 550 K) and α-$CsPbI_3$ (600 K), as measured on FOCUS with 4 Å incident wavelength neutrons. The GDOS have been normalized to the same number of vibrational modes in the energy range between 0 and 20 meV. The black dashed lines indicate a ω^2 Debye law from acoustic phonons.

D. Temperature dependence of the phonons in $\delta-CsPbI_3$

Figure S6 shows $S(\omega)$ (summed over q), and the corresponding $\chi''(\omega) = S(q,\omega)/(1 + n(\omega))$, for $\delta-CsPbI_3$ for different temperatures from 10 K up to close to the phase transition to the $\alpha-$phase. As can be seen, only a weak temperature dependence is observed. In Fig. S6 (b) the phonon population is accounted for, and the decreasing intensity with increasing

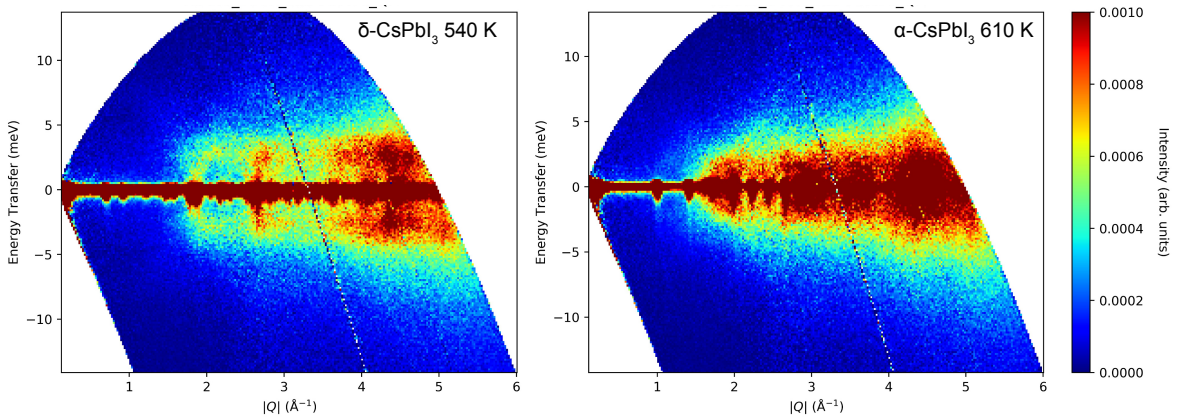

FIG. S5. $S(q,\omega)$ of δ-$CsPbI_3$ (left panel) and α-$CsPbI_3$ (right panel), as measured on ARCS using an incident neutron energy of 15 meV.

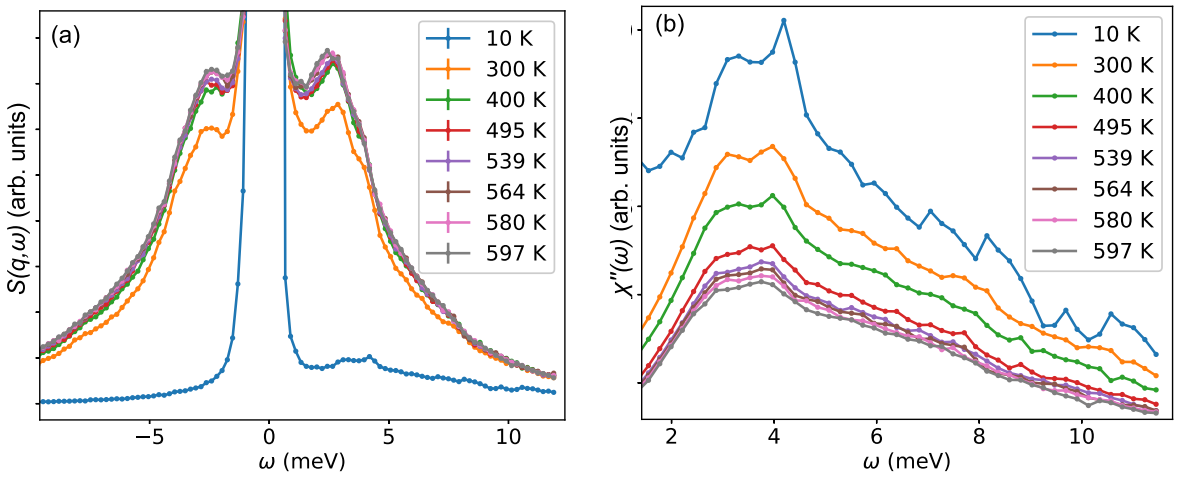

FIG. S6. $S(\omega)$ of δ-$CsPbI_3$ as a function of temperature, and in (b) the corresponding $\chi(\omega)$ accounting for the different phonon population for different temperatures. The data was integrated over q between $1.5-5$ Å^{-1}.The data was measured on ARCS using an incident neutron energy of 15 meV.

temperature is due to the increasing Debye-Waller factor.

E. Momentum transfer dependence of the INS signal

Figure S7 shows the $S(q)/q^2$ integrated over the energy interval $[1,3]$ meV for δ-$CsPbI_3$ and α-$CsPbI_3$. The intensity is divided by q^2 to remove the trivial q^2 increase of phonon scattering. At 540 K, in the δ-phase, $S(q)/q^2$ exhibits a decreasing behaviour with q superimposed with an oscillatory behaviour with local maxima at around 1.9, 2.6, 3.9, and 4.4 Å^{-1}. Such a behaviour is typical for coherent scatterers where the q-behaviour is determined from both an atomic correlation phase factor ($\exp(i\mathbf{q}\cdot\mathbf{r}_j)$) and also the scalar product of $\mathbf{q}$ and the phonon eigenvector [S11]. We note that the overall behaviour of $S(q)/q^2$ is rather similar for both phases, however, there are some important differences. In α-$CsPbI_3$ at 610

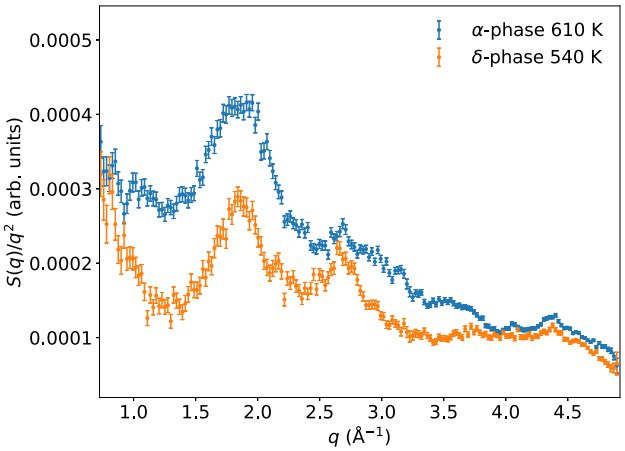

FIG. S7. $S(q)/q^2$ integrated over the energy interval from 1 to 3 meV for δ-$CsPbI_3$ and α-$CsPbI_3$. The data were measured at ARCS using an incident neutron energy of 15 meV.

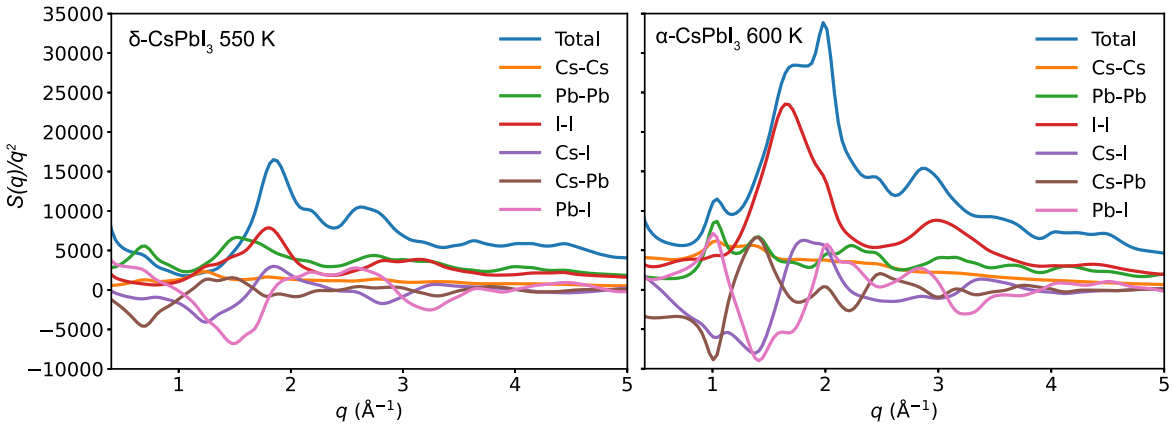

FIG. S8. $S(q)/q^2$ integrated over the energy interval from 0.1 to 3 meV for δ-$CsPbI_3$ and α-$CsPbI_3$, as obtained from the MD simulations. The partial contributions are also shown.

K, this oscillatory behaviour persists, although with slightly broader oscillatory features. Figure S8 shows the corresponding data as obtained from the MD simulations. Shown is also the partial contributions from different atomic correlations. One may note that the Cs-Cs correlations are basically incoherent above ≥ 1.6 Å^{-1} in the $\alpha-$phase. This is more clearly shown in Fig. S9 which shows the partial contributions to $S(q)/q^2$ in the $\delta-$ and $\alpha-$phases.

F. Fitting of $S(q,\omega)$ for cubic perovskites phases

Fitting of the spectra for $\alpha-CsPbI_3$ at $q = 2.35$ Å^{-1} and $q = 2.55$ Å^{-1} are shown in Figure S10. As can be seen, no overdamped dynamics can be observed at these q-points. An illustration of the parts of the $q-$ space probed with the powder INS for $q = 1.55$ Å^{-1} and $q = 1.85$ Å^{-1} is shown in Fig. S12. The illustration is a plot of the $L = 0$ plane, and the Brillouin zones are marked as solid black lines.

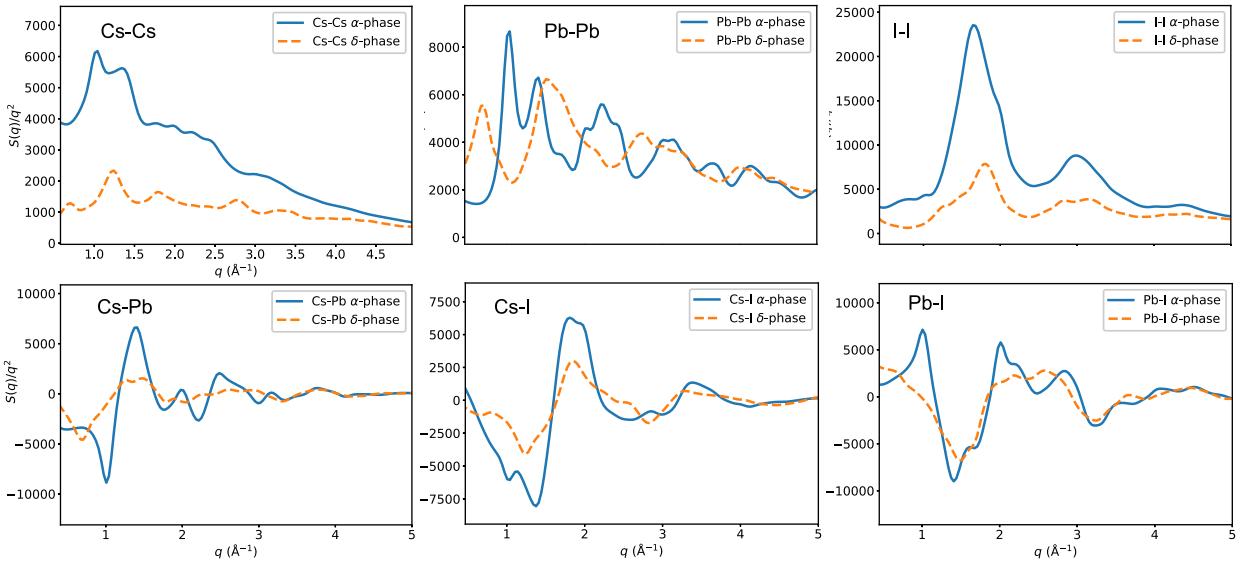

FIG. S9. MD simulated $S(q)/q^2$, integrated over the energy interval from 0.1 to 3 meV, for the different atomic contributions for the $\delta-CsPbI_3$ at 550 K and $\alpha-CsPbI_3$ at 600 K.

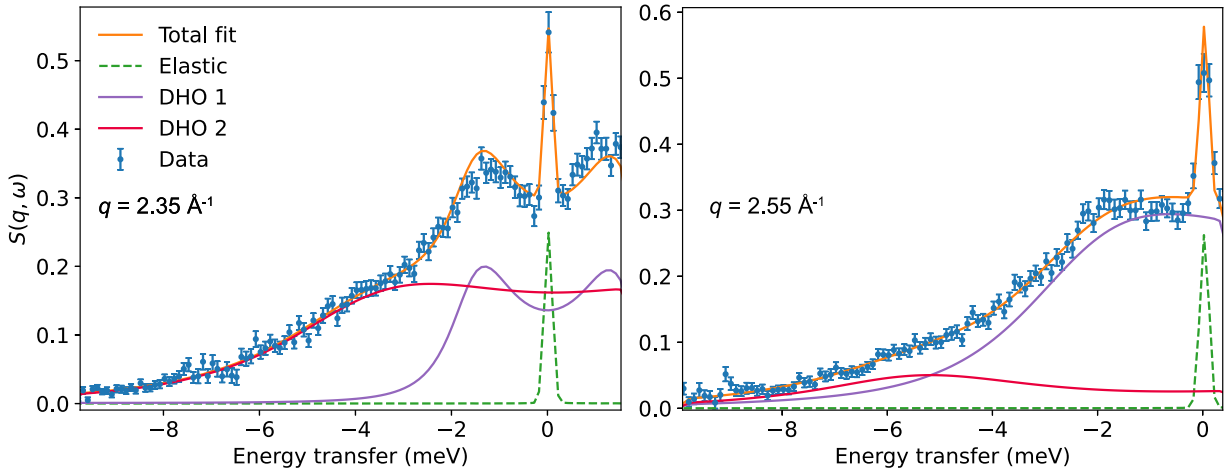

FIG. S10. Fitting of the INS spectra of α-$CsPbI_3$ at 600 K. The data were measured on FOCUS with an incident neutron wavelength of 4 Å.

G. INS results on $CsPbBr_3$

The $S(q,\omega)$ of $CsPbBr_3$ measured at $q = 1.69$ Å^{-1}, roughly corresponding to the modulus of M, as measured on FOCUS with an incident neutron wavelength of 4 Å is shown in Fig. S13. Quasielastic scattering is observed in the tetragonal $\beta-$ and cubic $\alpha-$phases, whereas in the orthorhombic $\gamma-$phase at 300 K, no quasielastic scattering is observed. The spectra can be, similarly to the spectra of $CsPbI_3$, as described in the main paper, be fitted to an elastic component, a quasielastic Lorentzian component, and one damped harmonic oscillator component. The FWHM of the Lorentzian component increases with increases with increasing temperature, and evolves from 0.32 meV at 400 K to 0.57 meV at the

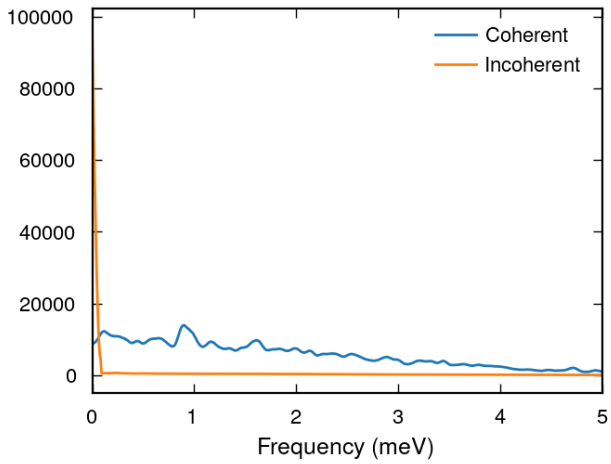

FIG. S11. MD simulated $S(q,\omega)$ at $q = 1.7$ Å^{-1} with both coherent and incoherent contribution. The data is convoluted with a Gaussian of FWHM 0.1 meV. Note that the incoherent mainly contributes to the elastic scattering, whereas the inelastic contribution is negligible.

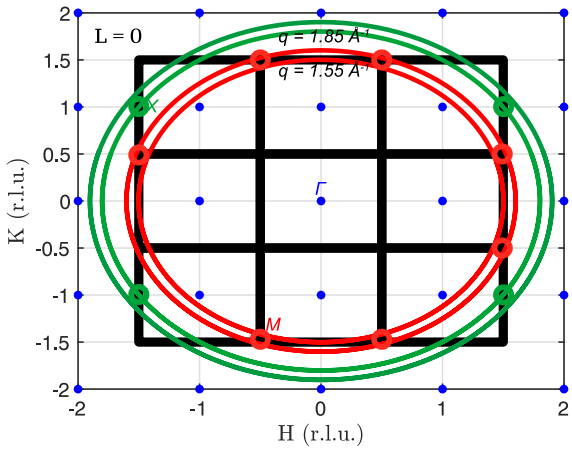

FIG. S12. Illustration of the parts of $q-$space probed with the powder INS for $q = 1.55$ Å^{-1} and $q = 1.85$ Å^{-1}, which is marked as the volume between the red and green lines, respectively. The illustration is a plot of the $L = 0$ plane and the Brillouin zones are marked as solid black lines.

highest measured temperature of 520 K, which corresponds to relaxation times (calculated as $2\hbar$/FWHM) between $4.2 - 2.3$ ps.

S3. SUPPLEMENTARY SIMULATION DATA

A. Cross-terms of simulated $S(q,\omega)$

The cross-correlation terms of the MD simulated partial dynamical structure factor are shown in Figure S14. Notice that the partial contributions can be negative for some energy and wavevector ranges, but the total $S(q,\omega)$ is always positive. The MD simulated $S(q,\omega)$ at the $M-$point of the Brillouin zone is shown in Figure S15.

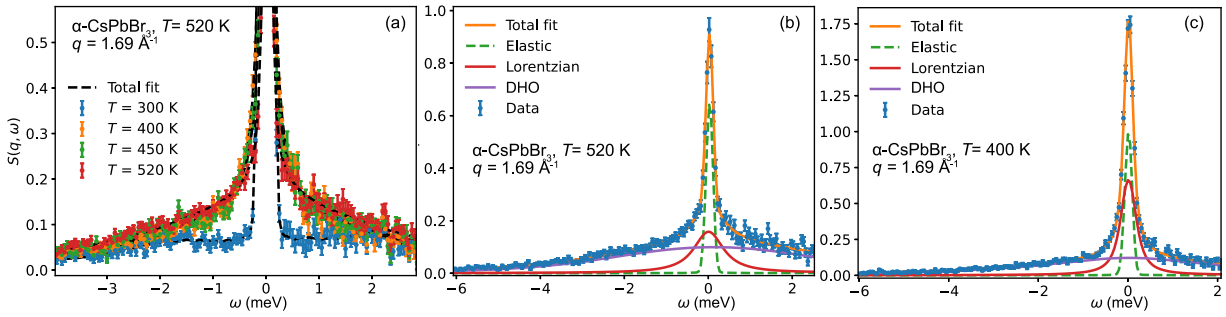

FIG. S13. (a) $S(q,\omega)$ for $CsPbBr_3$ at $q = 1.69$ Å^{-1} for different temperatures. The observed quasielastic scattering is assigned to the M-point overdamped octahedral tilting mode. (b-c) Fitting of the data for 520 K and 400 K. The data was measured on FOCUS using an incident neutron wavelength of 4 Å.

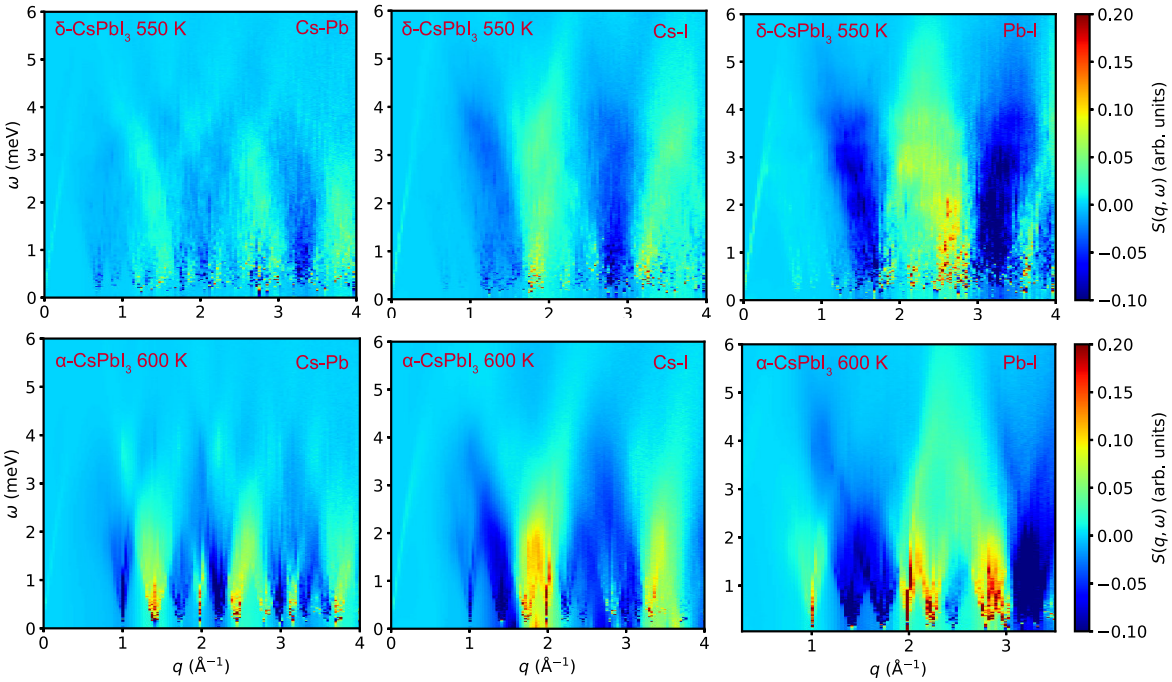

FIG. S14. Cross terms of the MD simulated partial dynamical structure factor for δ-$CsPbI_3$ at 550K (top panels) and α-$CsPbI_3$ at 600K (bottom panels), as calculated from the MD simulations. Note that the partial $S(q,\omega)$s can be negative, but the total $S(q,\omega)$ is always positive.

B. Analysis of relaxational dynamics in simulated $S(q,\omega)$ and Comparison of single crystal and powder simulations

Figure S16 compares the MD simulated partial I-I $S(q,\omega)$ at $M = (3/2, 1/2, 0)$ and the corresponding powder averaged $S(q,\omega)$ at $q = 1.57$ Å^{-1}. Note that the broad peaks centered around ~ 1.2 meV, is only present in the powder averaged $S(q,\omega)$. The observed relaxational dynamics was fitted to a Lorentzian function for with a HWHM of about 0.15 meV at the

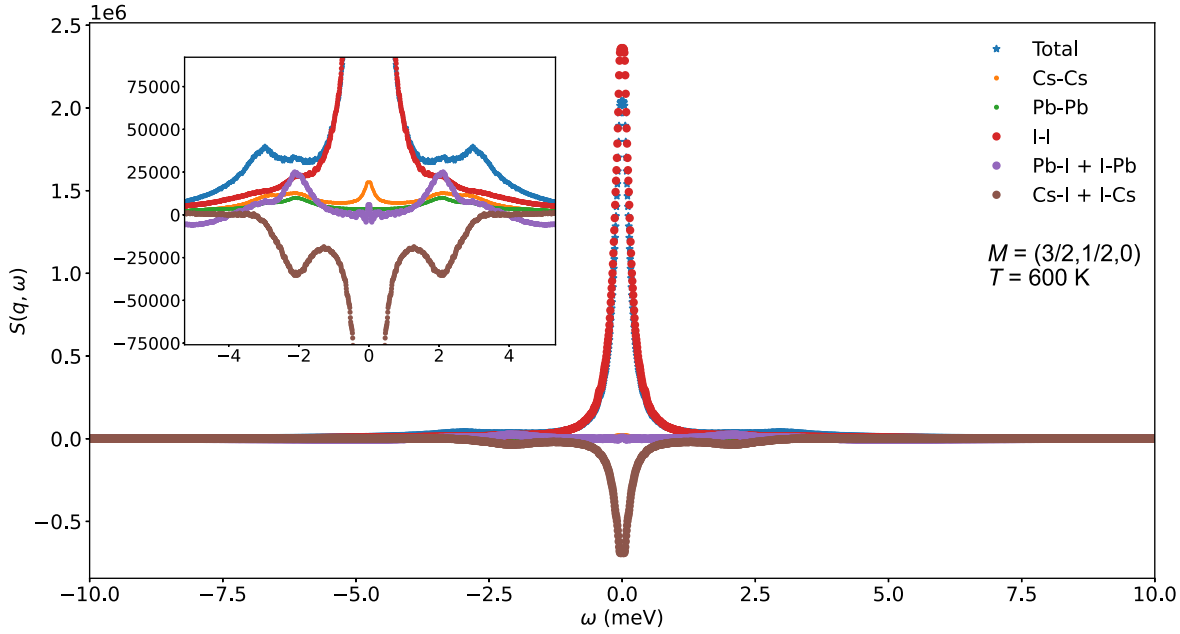

FIG. S15. Partial dynamical structure factor simulated at the M point. The inset shows a close-up of the different atomic contributions. Note that Cs−I shows a strong anti-correlation. The negative frequency side is a mirror image of the positive frequency side, *i.e.* $S(q, -\omega) = S(q, \omega)$.

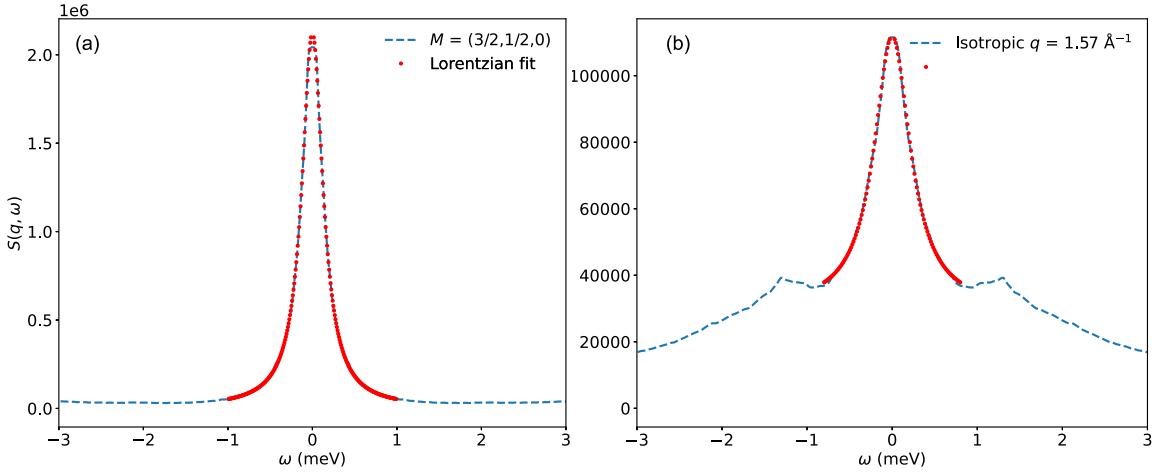

FIG. S16. MD simulated partial I-I $S(q, \omega)$ for (a) at $M = (3/2, 1/2, 0)$ and (b) the corresponding powder averaged $S(q, \omega)$ at $q = 1.57$ Å^{-1}. The observed relaxational dynamics was fitted to a Lorentzian function for with a HWHM of about 0.15 meV for (a) and 0.24 meV for (b). The negative frequency data is a mirror image of the positive frequencies, *i.e.* $S(q, -\omega) = S(q, \omega)$.

M-points and 0.24 meV for the powder averaged $S(q, \omega)$ at $q = 1.57$ Å^{-1}.

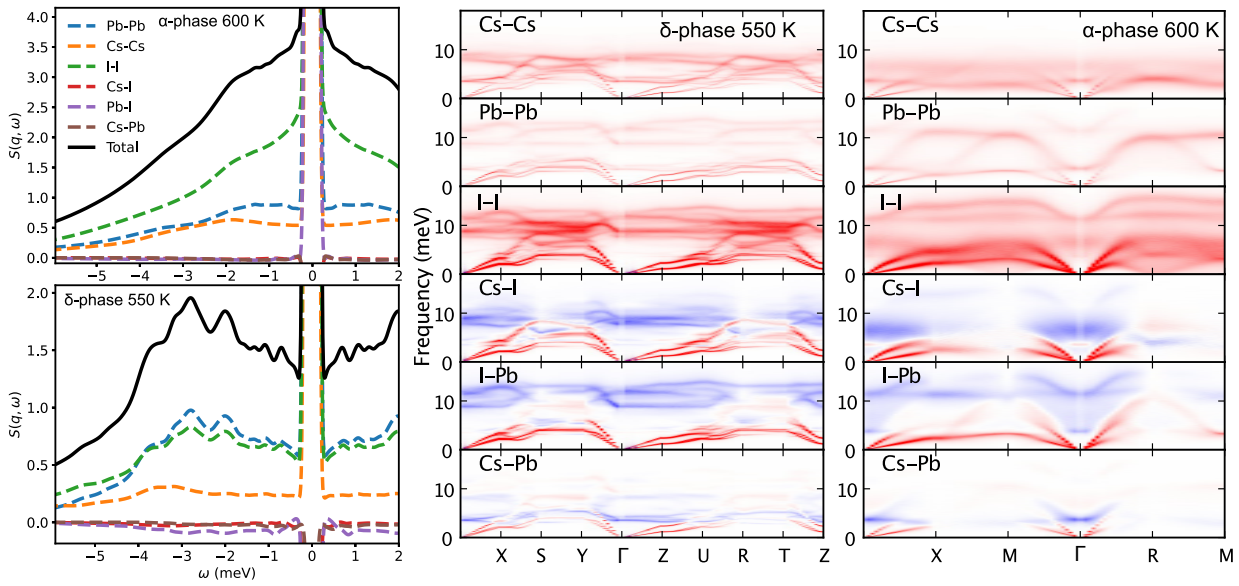

FIG. S17. (Left panel) Partial dynamic structure factors of δ-$CsPbI_3$ at 550 K (bottom) and α-$CsPbI_3$ at 600 K (top) as derived from MD simulations, summed over q from 0.2−3 $Å^{-1}$. Current correlations for δ-$CsPbI_3$ at 550 K (mid panel) and α-$CsPbI_3$ at 600 K (right panel) as derived from MD simulations, plotted along the high symmetry directions. Note that red and blue colors shows positive and negative values, respectively.

(S1) Dastidar, S.; Hawley, C. J.; Dillon, A. D.; Gutierrez-Perez, A. D.; Spanier, J. E.; Fafarman, A. T. Quantitative Phase-Change Thermodynamics and Metastability of Perovskite-Phase Cesium Lead Iodide. *J. Phys. Chem. Lett.* **2017**, *8*, 1278–1282.

(S2) Wang, B.; Novendra, N.; Navrotsky, A. Energetics, Structures, and Phase Transitions of Cubic and Orthorhombic Cesium Lead Iodide ($CsPbI_3$) Polymorphs. *J. Am. Chem. Soc.* **2019**, *141*, 14501–14504.

(S3) Arnold, O. et al. Mantid - Data analysis and visualization package for neutron scattering and μ SR experiments. *Nucl. Instruments Methods Phys. Res. Sect. A Accel. Spectrometers, Detect. Assoc. Equip.* **2014**, *764*, 156–166.

(S4) Abernathy, D.; Goyette, R.; Granroth, G. ARCS White Beam Vanadium Normalization for SNS Cycle 2021B. Date of Access: 2024-08-25, 2024; doi:10.14461/oncat.data.65a97b8585f57928f1f67178/2281898.

(S5) Miskowiec, A.; Spano, T.; Brubaker, Z. E.; Niedziela, J. L.; Abernathy, D. L.; Hunt, R. D.; Finkeldei, S. Antiferromagnetic ordering and possible lattice response to dynamic uranium valence in U_3O_8. *Phys. Rev. B* **2021**, *103*, 205101.

(S6) Nix, F.; MacNair, D. The thermal expansion of pure metals: copper, gold, aluminum, nickel, and iron. *Phys. Rev.* **1941**, *60*, 597–605.

(S7) Liu, J.; Phillips, A. E.; Keen, D. A.; Dove, M. T. Thermal Disorder and Bond Anharmonicity in Cesium Lead Iodide Studied by Neutron Total Scattering and the Reverse Monte Carlo Method. *J. Phys. Chem. C* **2019**, *123*, 14934–14940.

(S8) Marronnier, A.; Roma, G.; Boyer-Richard, S.; Pedesseau, L.; Jancu, J.-M.; Bonnassieux, Y.; Katan, C.; Stoumpos, C. C.; Kanatzidis, M. G.; Even, J. Anharmonicity and Disorder in the Black Phases of Cesium Lead Iodide Used for Stable Inorganic Perovskite Solar Cells. *ACS Nano* **2018**, *12*, 3477–3486.

(S9) Chazallon, B.; Itoh, H.; Koza, M.; Kuhs, W. F.; Schober, H. Anharmonicity and guest-host coupling in clathrate hydrates. *Phys. Chem. Chem. Phys.* **2002**, *4*, 4809–4816.

(S10) Squires, G. L. *Introduction to the Theory of Thermal Neutron Scattering*; Cambridge University Press, New York, 1978.

(S11) Fabiani, E.; Fontana, A.; Buchenau, U. Neutron scattering study of the vibrations in vitreous silica and germania. *J. Chem. Phys.* **2008**, *128*, 244507.